Accepted Manuscript

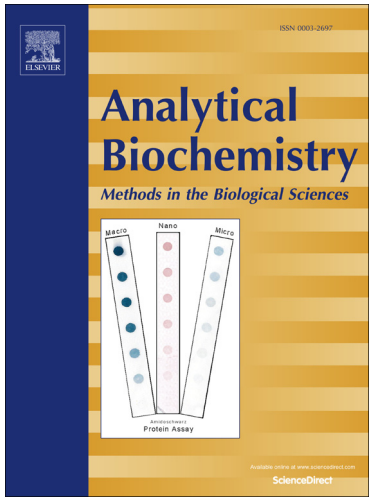

Electrocatalytic activity of core-shell magnetic nanocomposite

Rong Tian, Xiaojun Chen, Xiaolong Xu, Cheng Yao

PII: S0003-2697(14)00278-4
DOI: http://dx.doi.org/10.1016/j.ab.2014.06.019
Reference: YABIO 11784

To appear in: *Analytical Biochemistry*

Received Date: 12 May 2014
Revised Date: 19 June 2014
Accepted Date: 23 June 2014

Please cite this article as: R. Tian, X. Chen, X. Xu, C. Yao, Electrocatalytic activity of core-shell magnetic nanocomposite, *Analytical Biochemistry* (2014), doi: http://dx.doi.org/10.1016/j.ab.2014.06.019

Electrocatalytic activity of core-shell magnetic nanocomposite

Rong Tian, Xiaojun Chen*, Xiaolong Xu, Cheng Yao*

College of Science, Nanjing Tech University, Nanjing 211816, P R China

Running title: Detecting H_2O_2 based on electro-active magnetic nanocomposite

*Corresponding authors

Tel. &Fax: +86-25-58139482

E-mail addres: chenxj_njut@126.com (X Chen),

yaocheng@njtech.edu.cn (C Yao)

Abstract

Electrically active magnetic nanocomposites (EAMNC), Au nanoparticles/self-doped polyaniline@Fe_3O_4 (AuNPs/SPAN@Fe_3O_4) with well-defined core-shell structure, were first synthesized by a simple method. The morphology and composition of the as-synthesized AuNPs/SPAN@Fe_3O_4 nanocomposite have been characterized by transmission electron microscopy (TEM), scanning electron microscopy (SEM), Fourier-transform IR (FT-IR), UV-Vis, X-ray powder diffraction (XRD) and thermo-gravimetric analysis (TGA). Horseradish peroxidase (HRP)-AuNPs/SPAN@Fe_3O_4 biocomposites were immobilized onto the surface of ITO electrode to construct an amperometric hydrogen peroxide (H_2O_2) biosensor. The effects of HRP dosage, solution pH and the working potential on the current response toward H_2O_2 reduction were optimized to obtain the maximal sensitivity. Under the optimal conditions, the proposed biosensor exhibited a linear calibration response in the range of 0.05-0.35 mM and 0.35-1.85 mM, with a detection limit of 0.01 mM (signal/noise=3). The modified electrode could virtually eliminate the interference of ascorbic acid (AA) and uric acid (UA) during the detection of H_2O_2. Furthermore, the biosensor was applied to detect H_2O_2 concentration in real samples, which showed acceptable accuracy with the traditional potassium permanganate titration.

Keywords: magnetic nanocomposites; self-doped polyaniline; horseradish peroxidase; hydrogen peroxide; electrocatalysis

Introduction

Magnetic nanoparticles have become attractive for exploitation mainly in information storage, ferrofluids, color imaging, drug targeting and delivery, cancer therapy, separations, and catalysis [1-6]. As a representative example, magnetite (Fe_3O_4) has been extensively studied. However, due to the magnetic dipolar-dipolar attraction, Fe_3O_4 nanoparticles incline to aggregate into clusters; additionally, the Fe_3O_4 nanoparticles with relatively small sizes may undergo rapid biodegradation upon directly exposing to the biological environments [7]. Therefore, the surface modification with various useful materials during the synthesis or coating process of superparamagnetic Fe_3O_4 nanoparticles might be helpful to overcome these limitations.

In recent years, the core/shell structured magnetic nanocomposites with Fe_3O_4 as the core and inorganic materials or polymers as the shell have been extensively proposed. These specific core/shell materials possess the ability to be modified with different charges, functions or reactive moieties on the surface with enhanced stability and compatibility, and provide an avenue for the synthesis of complex nanocomposites. Moreover, these nanocomposites usually combine with the advantageous properties of both core and shell, and are promisingly applied as electrocatalysts, drug delivery, and fluorescent biological labels [8-10]. For example, Jang et al. have synthesized human natural killer cells (NK-92MI) loaded Cy5.5-SiO_2@Fe_3O_4 core/shell nanocomposites, which could be infiltrated into the target tumor site by an external magnetic field [11]. Govindaiah and his coworkers

have shown that Fe_3O_4/poly(fluorescein o-methacrylate) magnetic fluorescent nanocomposites can be used in bioimaging by visualizing the cellular uptake of the nanocomposites into A549 lung cancer cells [12]. Thus, the synthesis of multifarious magnetic core/shell nanocomposites with multiple properties attracts more and more attentions.

Among these shell materials, polyaniline (PANI) has been widely investigated. As both electrical conductor and organic compound, PANI possesses flexibility, robustness, highly controllable properties, simple synthesis, low cost, and environmental stability. Fe_3O_4-PANI core/shell nanocomposites which exhibit the properties of both constituents, magnetic as well as conducting, have proved to have many applications like chromatographic solid extraction [13], protein digestion [14], catalyst [15], etc. In addition, based on the excellent electrochemical behavior of PANI and on the good biocompatibility of Fe_3O_4, the resultant Fe_3O_4-PANI core/shell nanocomposites might be used to construct a kind of biosensor in which the mediators could be omitted and the fabrication of the biosensors could be greatly simplified.

In this paper, electrochemically active self-doped PANI@Fe_3O_4 (SPAN@Fe_3O_4) core/shell nanocomposite was one-pot synthesized from Fe_3O_4, aniline (AN) and 3-aminobenzenesulfonic acid (SAN). It was not only manipulated easily by an external magnetic field, but also possessed electro-activity of PANI extending to neutral medium due to the effective doping of sulfonic acid groups. On the other hand, it is well-known that Au nanoparticles (AuNPs) were safe in both animals and humans, and they also exhibited good biocompatibility and affinity via amine/thiol terminal

groups [16]. Then, AuNPs were modified on the surface of SPAN@Fe_3O_4 through electrostatic adsorption, and the ratio of Au in the AuNPs/SPAN@Fe_3O_4 composites was estimated as about 29.7 % via thermo-gravimetric analysis (TGA). The synthetic process of AuNPs/SPAN@Fe_3O_4 nanocomposites was simple, and to our knowledge, there is no report of such nanocomposites with multifunction of biocompatiblity, electro-activity, conductivity and magnetism. As an example, horseradish peroxidase (HRP) was successfully immobilized on AuNPs/SPAN@Fe_3O_4 modified ITO electrode. For the first time an amperometric H_2O_2 biosensor was fabricated on the basis of HRP-AuNPs/SPAN@Fe_3O_4 modified electrode.

Experimental Section

Materials

Ferric chloride hexahydrate ($FeCl_3 \cdot 6H_2O$), sodium acetate (NaAc), polyethylene glycol (PEG) 10000, ammonium persulfate ($(NH_4)_2S_2O_8$, APS) were purchased from Shanghai Linfeng Chemical Reagent Co. Ltd., China. Poly(vinylpyrrolidone) (PVP, 30 kDa) and poly(diallyldimethylammonium chloride) (PDDA, 20 wt %) were purchased from Aldrich. Stock solution of 3 % PDDA was prepared in double distilled water with Tris and NaCl. Aniline (AN) was distilled twice under reduced pressure and stored in dark at low temperature before use. 3-aminobenzenesulfonic acid (SAN) was purchased from TCI. Chloroauric acid hydrated ($HAuCl_4 \cdot 4H_2O$) was purchased from Nanjing Chemical Reagent Co. Ltd., China. H_2O_2 (30 % w/v solution) was obtained from Sinopharm Chemical Reagent Co. Ltd., and its accurate

concentration was determined by titration with potassium permanganate. Phosphate buffer saline (PBS, 0.1 M) was prepared by mixing the stock solutions of KH_2PO_4 and K_2HPO_4, and adjusted to appropriate pH by addition of 0.1 M NaOH or H_3PO_4 solution. 250 U mg^{-1} HRP (EC 1.11.1.7), uric acid (UA) and ascorbic acid (AA) were all purchased from Sigma. Nafion (Nf) was obtained from DuPont as 5 wt % solution and used as 0.5 wt % solution after dilution with water. Potassium ferricyanide ($K_3[Fe(CN)_6]$), potassium ferrocyanide ($K_4[Fe(CN)_6]$) and potassium chloride (KCl) were from Shanghai Linfeng Chemical Reagent Co., Ltd., China. Other reagents were of analytical grade and used without further purification. Double distilled water was used throughout the experiments.

Characterization

The structures and morphologies of the Fe_3O_4, SPAN@Fe_3O_4 and AuNPs/ SPAN@Fe_3O_4 were characterized by Philip-X'Pert X-ray diffractometer taken with a Cu KR X-ray source, transmission electron microscopy (TEM, JEOL JEM-200CX) and field-emission scanning electron microscopy (FESEM, HITACHI S4800). Fourier transform infrared (FT-IR) spectra of KBr powder-pressed pellets were recorded on a Bruker model VECTOR22 Fourier-transform spectrometer. UV–Vis spectra were recorded on Agilent UV–Vis spectrophotometer. TGA was performed on NETZSCH STA 449C. Zeta potential analysis was performed with a PALS Zeta Potential Analyzer, version 3.43 (Brookhaven Instruments Corp.). The static water contact angles were measured at 25 ℃ by a contact angle meter (Rame-Hart-100)

using drops of pure deionized water. The readings were stabilized and taken within 120 s after the addition. The magnetic properties of the samples were measured using a 7-T Quantum Design superconducting quantum interference device (SQUID) magnetometer. The zero-field cooled (ZFC) and field-cooled (FC) measurements were performed by cooling the sample to 5 K at zero field or in the presence of an external field of 100 Oe, respectively. All the magnetic measurements during the warming runs were carried out in a field of 100 Oe.

Cyclic voltammetry (CV), electrochemical impedance spectroscopy (EIS) and amperometric measurements were performed using a CHI660D electrochemical workstation (Shanghai CH Instruments, China). A three-compartment electrochemical cell contained a saturated calomel reference electrode (SCE) against which all potentials were measured, a platinum wire auxiliary electrode and the modified ITO magnetism-electrode (Φ = 3 mm) working electrode. The CV and EIS characterizations were performed in 0.1 M KCl solution containing 5 mM $[Fe(CN)_6]^{3-/4-}$ (1:1). The determination of H_2O_2 was conducted in 0.1 M PBS. The sensor responses were measured as the difference between total and residual currents.

Preparation of AuNPs/SPAN@Fe_3O_4 magnetic nanocomposite

The magnetic Fe_3O_4 microspheres were prepared through a solvothermal reaction (see in Supporting information) [17]. Core-shell structured SPAN@Fe_3O_4 magnetic nanocomposite was prepared as follows: 0.3 g of PVP and 0.06 g of Fe_3O_4 nanoparticles were dispersed into 66 mL of H_2O under ultrasonication at room

155 temperature for 30 min. Then, 28.2 μL AN and 0.05 g SAN with 9 mL of 0.2 M HCl
156 were added into the mixture, followed by adding 60 mL of H_2O. After the solution
157 was shaken for 30min, the oxidant APS with a concentration of 0.06 M was added
158 drop by drop to start the copolymerization reaction under vigorous stirring and the
159 reaction was allowed to proceed for 8 h at 4 □. After the reaction, the precipitate was
160 magnetic separated and washed successively with H_2O and ethanol three times, and
161 then dried under vacuum at 60 □ for 6 h for further use.

162 An electrostatic attraction method was employed for the immobilization of
163 AuNPs onto the SPAN@Fe_3O_4 core/shell nanocomposite to form the
164 AuNPs/SPAN@Fe_3O_4 magnetic nanocomposite. In order to induce positive charges at
165 the surface of the SPAN@Fe_3O_4 nanocomposite, 10 mg of SPAN@Fe_3O_4 was
166 dispersed in 4 mL H_2O with 1 mL 3 % PDDA aqueous solution, and the mixture was
167 sonicated for 3 min. The residual PDDA was removed by magnetic separation and the
168 nanocomposite was rinsed with water at least three times. Subsequently, the positively
169 charged SPAN@Fe_3O_4 nanocomposite was added to 30 mL of Au colloid solution and
170 stirred for 8 h. The AuNPs were electrostatically attracted on the surface of the
171 SPAN@Fe_3O_4 nanocomposite. Finally, the resultant dark-purple AuNPs/
172 SPAN@Fe_3O_4 product was removed from the solution by applying an external
173 magnetic field and the supernatant liquor was colorless. After washed with water and
174 ethanol for three times, the AuNPs/SPAN@Fe_3O_4 nanocomposite was dried under
175 vacuum at 50 □ for 6 h.

176

Fabrication of Nf-HRP-AuNPs/SPAN@Fe_3O_4 modified ITO magnetism electrode

Before modification, the ITO chips were cleaned with acetone, ethanol and water in turn, and then dried under a stream of nitrogen. A 2-mm-thick poly (dimethylsiloxane) (PDMS) with a circular opening of 3-mm diameter formed from a predefined mold was bound to the ITO surface to confine the active electrode area. The other side of the ITO was adhered to one terminal of a piece of NdFeB permanent magnet (8 mm diameter and 5 mm height). A silica rubber adhesive (Nanda 704, China) was used to seal the magnet. 10 μL of 2 mg mL^{-1} HRP solution was mixed with 10 μL of 10 mg mL^{-1} AuNPs/SPAN@Fe_3O_4 nanocomposite in 0.5 % Nf dispersion to form a homogenous mixture. Then, 10 μL of the mixture was dried on the surface of ITO magnetism-electrode under ambient condition, which was designated as Nf/HRP-AuNPs/SPAN@Fe_3O_4/ITO. When the biosensor was not in use, it was stored at 4 ℃ in a refrigerator.

Results and discussion

Structure and composition characterization of samples

The morphologies of the resultant nanocomposites were studied by TEM and FESEM. The TEM in Fig. 1A of the Fe_3O_4 nanoparticles indicated that the sample is a bit agglomerated with the average diameter of ~380 nm. The presence of SPAN shells prevented agglomeration of the Fe_3O_4 nanoparticles, and hence the as-prepared SPAN@Fe_3O_4 nanocomposites were well dispersed on the copper grid with the average diameter of ~440 nm, as shown in Fig. 1B. The diameter of SPAN@Fe_3O_4

nanocomposites was increased by ~60 nm, demonstrating that the SPAN shell was ~30 nm thick. Fig. 1C shows the TEM image of AuNPs-Fe_3O_4@SPAN nanocomposites, and it is clear that the composite particles are constituted of three distinct components: a black core of Fe_3O_4, a gray shell of SPAN and an outermost layer of many tiny AuNPs (the dark spots in the image).

The FESEM images (Fig. 1D-F) further confirm the above results. From Fig. 1D of the Fe_3O_4 sample, it can be clearly seen that Fe_3O_4 particle is composed of many nearly monodisperse spherical particles and its surface is not smooth. FESEM image of the SPAN@Fe_3O_4 sample, as shown in Fig. 1E, indicates that the SPAN@Fe_3O_4 nanocomposite has a smooth SPAN shell. Fig. 1F shows that the AuNPs with a diameter of ~20 nm are immobilized evenly onto the surface of SPAN@Fe_3O_4 nanocomposites. Moreover, the AuNPs/SPAN@Fe_3O_4 hybrid composite structures are stable enough and not disintegrated even after sonicating for 2 h.

Fig. 1

XRD and FT-IR spectra are used to characterize the chemical structure of the obtained samples. The XRD pattern of the as-synthesized Fe_3O_4 is shown in curve a of Fig. 2A, the diffraction peaks at $2\theta = 30.1°$, 35.6°, 37.2°, 43.1°, 53.5°, 57.1° and 62.7° are observed, which can be indexed to face-center-cubic phase of Fe_3O_4 (JCPDS 75-1609). Based on the XRD pattern (311), the average crystallite size of Fe_3O_4 nanoparticles deduced from the Scherrer equation is about 15 nm. According to the

representative TEM and FESEM images of Fig. 1A and 1D, the average size of Fe_3O_4 nanospheres is about 380 nm. The discrepancy between the XRD and TEM/FESEM data could be understood by assuming that the 380 nm-sized particles were actually composed of 15 nm-sized Fe_3O_4 nanoparticles. This suggests that Fe_3O_4 nanoparticles have self-assembled into spherical aggregates. In fact, a close look at the FESEM image indicated that large particle is an assembly of many small Fe_3O_4 nanocrystals, and disordered pores exist among the primary nanoparticles but within spherical aggregates. Furthermore, the typical XRD peaks of pure Fe_3O_4 nanospheres are also observed in SPAN@Fe_3O_4 (curve b) and AuNPs/SPAN@Fe_3O_4 (curve c) nanocomposites, indicating that the outer SPAN shell and AuNPs did not result in the crystallinity change of inner Fe_3O_4 nanospheres. The absence of SPAN peak in the XRD pattern in the SPAN@Fe_3O_4 sample is due to its amorphous structure coated on the Fe_3O_4 nanospheres. Curve c shows a XRD pattern of the AuNPs/SPAN@Fe_3O_4 sample. In addition to the diffraction peaks that correspond to Fe_3O_4, there also exists two other diffraction peaks (labeled with the symbol #). The position and intensity of the diffraction peaks match well with (111) and (200) crystal faces of cubic phase Au (JCPDS 04-0783). The diffraction peaks are broadening, which indicates that the Au product is also composed of small particles.

Fig. 2B shows the FT-IR spectra of Fe_3O_4 (curve a), SPAN@Fe_3O_4 nanocomposites (curve b) and AuNPs/SPAN@Fe_3O_4 (curve c) samples. Compared with the previous report [18], the absorption of the Fe-O vibration shifted to a higher wave number of 590 cm^{-1}. A basic effect of finite size of nanoparticles is the breaking of a large

number of bonds for surface atoms resulted in the rearrangement of unlocalized electrons on the particle surface. As a result, when particles were reduced to nanoscale dimensions, the absorption bands of FT-IR spectra shift to higher wave number [19]. The bands appeared near 1612 and 3415 cm^{-1} are related to the H-O-H bending mode and the O-H stretching vibrations, respectively, indicating the presence of interstitial water in the samples [20]. The two bands located at 1550 and 1405 cm^{-1} correspond to the COO^- anti-symmetrical vibration and COO^- symmetric vibration, indicating the bidentate bonding of the carbonyl groups to the surface Fe atoms [15]. Actually, the carboxyl group functionalized Fe_3O_4 nanospheres are "negatively" charged with a ζ-potential of −2.3 mV. Curve b shows the typical FT-IR spectrum of SPAN@Fe_3O_4 nanocomposites, all of the characteristic peaks of SPAN were displayed. In detail, the peaks at 1640 and 1458 cm^{-1} are characteristic of the C=C stretching vibration of quinoid and benzenoid rings, respectively. The C–N stretching of secondary aromatic amines (1274 cm^{-1}), and the aromatic C–H bending (1218 cm^{-1}) are also observed. The bands at 1087, 686 and 614 cm^{-1} are attributed by the O=S=O, S–O and C–S stretching vibration, respectively. Moreover, the peak observed at 833 cm^{-1} reveal the presence of 1, 2, 4-trisubstitution of aromatic ring [21]. These peaks further proved that the SPAN shell is successfully coated on the Fe_3O_4 microsphere surface. Curve c shows the FT-IR spectrum of AuNPs/SPAN@Fe_3O_4 nanocomposites. Because AuNPs do not have absorption in the infrared region, the characteristic peak of AuNPs/SPAN@Fe_3O_4 sample is almost the same as that of SPAN@Fe_3O_4.

Due to the large amount of $–SO_3H$ functional groups doped on the surface of SPAN,

the SPAN@Fe_3O_4 nanocomposites were negative charged with a ζ-potential of -8.3 mV. After SPAN@Fe_3O_4 nanocomposites achieved positive charged modification using PDDA solution, they could be immobilized with negatively charged, citrate-coated AuNPs by electrostatic interactions. Fig. 2C shows the UV-Vis absorption spectra of the colloidal Au solution (curve a) and the Au solution after magnetic separation of reacted AuNPs/SPAN@Fe_3O_4 nanocomposites (curve b). The characteristic UV-Vis absorption peak of the citrate-coated AuNPs appears at 515 nm. A dramatic decrease in the intensity at 515 nm is observed after the AuNPs deposition, indicating that almost all of the AuNPs are absorbed effectively on the positive charged SPAN@Fe_3O_4 surface. The fraction of the AuNPs in solution deposited on SPAN@Fe_3O_4 is up to 95%, which can be calculated by UV adsorption. Moreover, the color transformation from red to colorless after the immobilization reaction also indicates the success of effective immobilization. The energy-dispersive spectrum (EDS) analysis (Fig. 2D) also proves that the elemental compositions of the nanocomposites are Fe, C, O, N, S and Au, which agree with the XRD analysis. All the above results indicate that mono-dispersed AuNPs/SPAN@Fe_3O_4 nanocomposites have been formed.

Fig. 2

TGA was used to determine the weight percentage of Au in the AuNPs/ SPAN@Fe_3O_4, as shown in Fig. 3 (curve b). For comparison, the TGA curve of

SPAN@Fe_3O_4 was also presented as curve a. The weight loss in the first step is attributed to the loss of residual water, and the second and third steps that starts at around 200 ℃ corresponds to degradation of SPAN chains [22]. The residual masses of Fe_3O_4@SPAN and Au-Fe_3O_4@SPAN were about 91% and 93.6%, respectively. The weight percentage of Au in the AuNPs/SPAN@Fe_3O_4 can be calculated as about 29.7%, which might be due to the strong electrostatic effect between PDDA functionalized SPAN@Fe_3O_4 and AuNPs.

Fig. 3

Magnetism characterization of samples

The saturation magnetization (M_s), coercivity and remanence magnetization are derived from the SQUID measurements for pure Fe_3O_4, SPAN@Fe_3O_4 and AuNPs/SPAN@Fe_3O_4 nanocomposites at 300 K. As shown in Fig. 4A, the typical superparamagnetic behaviors are observed at room temperature (300 K) for pure Fe_3O_4, SPAN@Fe_3O_4 and AuNPs/SPAN@Fe_3O_4 nanocomposites, where there is no pronounced hysteresis loops. Superparamagnetism is the responsiveness to an applied magnetic field without retaining any magnetism after removal of the applied magnetic field. With the superparamagnetic property, capillary blockage by aggregations formed by residual magnetism after removal of the applied field will be avoided. In the inset, we have plotted the same data in the field range of -1 to 1 kOe, which shows all the coecivities are in the range of 126 Oe. The value of the coecivity is almost the

same, indicating that the anisotropy energy of the magnetic particles is not much affected by the presence of SPAN and Au layers. All the three nanoparticles show a tendency to saturate at 5.5 kOe, and the M_s values are found to be 90.2, 70.9 and 56.3 emu/g, respectively. The consecutive reduction in M_s value could be attributed to the lower density of the magnetic component in the SPAN@Fe_3O_4 and AuNPs/SPAN@Fe_3O_4 nanocomposites. This also can be explained by taking into account the diamagnetic contribution of the SPAN and Au layers surrounding the magnetic cores. For pure Fe_3O_4, the M_s value (90.2 emu/g) is just less than that of the bulk magnetite (92 emu/g) [22], which might be attributed to the small particle size effect of as-synthesized Fe_3O_4 nanoparticles.

In order to confirm the onset of the superparamagnetic phase further, ZFC-FC magnetization measurements were performed for pure Fe_3O_4, SPAN@Fe_3O_4 and AuNPs/SPAN@Fe_3O_4 nanocomposites, respectively, in the temperature range of 5-300 K, with maximum applied field of 100 Oe. The divergence between ZFC and FC curves is a typical feature of superparamagnetism [23]. As shown in Fig. 4B, the superparamagnetism of the Fe_3O_4 were indeed preserved after subsequent SPAN encapsulation and surface modification with AuNPs.

Fig. 4

Characterization of nanocomposites modified ITO electrodes

The influence of potential scan rate (v) on the response of the AuNPs/SPAN@Fe_3O_4

modified ITO electrode in PBS was also investigated, as shown in Fig. 5A. The CV peak currents (i_{pa} and i_{pc}) increased linearly with the square root of scan rate ($v^{1/2}$) in the range of 20-600 mV s^{-1}, indicating a surface-controlled electrode process.

The influence of pH value of PBS solution on the electrochemical behavior of AuNPs/SPAN@Fe_3O_4 modified ITO electrode was also studied, as shown in Fig. 5B. It is well-known that pure PANI bears electro-activity only when the pH is lower than 4.0, while the electro-activity of the copolymer SPAN is greatly improved. In low pH solutions, two distinctly separate redox peaks were observed, corresponding to the leucoemeraldine to the conducting emeraldine and the emeraldine to the pernigraniline conversion, respectively. From pH 5.0 to 9.0, the two sets of peaks overlapped into one pair of peaks, that is the leucoemeraldine/pernigraniline reaction. The effective extension for the electrochemical activity of SPAN is due to the presence of $–SO_3H$ groups into backbone of PANI. Because the H^+ ion in $–SO_3H$ groups can take a role of "buffer" and maintain the local pH value to some extent in SPAN near the electrode surface, the SPAN can still exhibit electrochemical activity in solution with higher pH value.

The wetting properties of the material were also investigated by measuring the water contact angles (θ) of pure Fe_3O_4 and corresponding composites. Fig. 5C (a, b, c) compares the contact angles of pure Fe_3O_4 (θ=48°), AuNPs/SPAN@Fe_3O_4 nanocomposites (θ=39.2°), and the immobilization of HRP (θ=20.8°), respectively. It shows that the wettability of material increases significantly with the modified steps. The contact angle decreased from 48° to 39.2° with the encapsulation of SPAN and

353 the absorption of AuNPs, which improved hydrophilicity to the surface and might be
354 helpful for the immobilization of biolomolecules. As shown in Fig. 5C (c), after
355 immobilization of HRP molecules, the prepared bionic interface with 20.8° of the
356 contact angle certifies the combination of HRP with the AuNPs/SPAN@Fe_3O_4
357 nanocomposites.
358
359 **Fig. 5**
360
361 CV technique is used to evaluate the electrochemical performance of the modified
362 ITO electrodes (Fig. 6A). For the bare ITO electrode, a pair of well-defined oxidation
363 and reduction peaks were caused by the $[Fe(CN)_6]^{3-/4-}$ redox couples which were
364 noticed in forward and reverse scans (curve a). After the electrode was modified with
365 Nf/AuNPs/SPAN@Fe_3O_4 composite, a small decrease in peak current was observed
366 (curve b). The negatively charged property of Nf layer could hinder the diffusion of
367 negatively charged probe ions toward the electrode surface, then tended to reduce
368 current response. The immobilization of HRP on the electrode surface was
369 accompanied by a further decrease in the amperometric response (curve c), indicating
370 that the non-conductive enzyme molecules were incorporated on the Nf
371 /HRP-AuNPs/SPAN@Fe_3O_4/ITO.
372 EIS can provide useful information on the impedance changes of the electrode
373 surface during the fabrication process. The Nyquist plot of the EIS includes a
374 semicircular portion and a linear portion. The diameter of the semicircle is equal to

the electron-transfer resistance (R_{et}) which shows the electron-transfer kinetics of the redox probe. Meanwhile, the linear part corresponds to the diffusion process. Fig. 6B displayed the Nyquist plots of (a) bare ITO, (b) Nf/AuNPs/SPAN@Fe_3O_4/ITO and (c) Nf/HRP-AuNPs/SPAN@Fe_3O_4/ITO. The R_{et} value of the AuNPs/SPAN@Fe_3O_4/ITO (296 Ω, curve b) was much larger than that of the bare ITO (113 Ω, curve a), showing that the Nf encapsulated nanocomposite film blocked the electron transfer of the electrochemical probe. After immobilizing HRP, The R_{et} value of Nf/HRP-AuNPs/SPAN@Fe_3O_4/ITO was increased to 513 Ω (curve c), since the non-conductive HRP obstructed electron transfer between the electrode surface and the electrochemical probe.

Fig. 6

Optimization of experimental parameters

In order to maximize the detection sensitivity of the proposed H_2O_2 biosensor, we optimized various conditions, including HRP dosage, solution pH, the working potential of chornoamperometry and the temperature, via changing the examined condition while the others were fixed.

The effect of enzyme loading on the catalytic current for H_2O_2 oxidation was initially studied in the presence of 0.5 mM H_2O_2. Fig. 7A showed the response currents of the modified electrode with different enzyme loading. The response current increased sharply with increasing the enzyme loading to the maximal value of

10 μL, and tended to become steady with further increases in the HRP dosage. In terms of economy, 10 μL of HRP loading was used for further experiments.

The effect of solution pH on the electrocatalytic reduction of H_2O_2 was investigated. Fig. 7B showed that the pH dependence of the biosensor response was evaluated at 0.5 mM H_2O_2 over the pH range from 3 to 9. The maximum response current was observed at pH 6.0. Thus, the PBS with pH 6.0 was chosen as the supporting electrolyte for H_2O_2 detection.

The influence of the applied potential on the biosensor response was investigated in the potential range of −0.20 V to 0 V, as shown in Fig. 7C. The biosensor response to 0.5 mM H_2O_2 increased with the change of applied potential from 0 V to −0.10 V, and the highest response was obtained at −0.10 V. A further increase of negative potential resulted in decrease in current response and then −0.10 V was chosen as the working potential.

The result of the effect of temperature on biosensor performance was also presented in Fig. 7D. It showed that the current response of the modified electrode was enhanced with temperature increase. When the temperature was higher than 37 °C, the amperometric response decreased. This phenomenon may be attributed to that the enzyme is denatured gradually at higher temperatures.

Fig. 7

Amperometric response of H_2O_2 biosensor

The typical chronoamperometric response of the biosensor to successive increments of H_2O_2 over the range of 0.05-1.85 mM under the optimum conditions was shown in Fig. 8A. The time required to reach 95 % of the maximum steady-state current was within 5 s. The response current showed a good linear relationship with the increase of H_2O_2 concentration in the ranges of 0.05-0.35 mM and 0.35-1.85 mM, and a plateau in current response was observed for H_2O_2 concentration beyond 1.85 mM (Fig. 8B). The linear regression equations was Δi_p / μA = 0.067 + 13.99 c(H_2O_2) / mM (r = 0.997) and Δi_p / μA =3.198 + 5.902 c(H_2O_2) / mM (r = 0.995) with the sensitivities of 199.9 and 84.3 μA cm^{-2} mM^{-1}, respectively. The detection limit was 0.01 mM at a signal-to-noise ratio of 3. According to the linear equation, H_2O_2 concentration could be detected quantitatively. The performance of the Nf/HRP-AuNPs/SPAN@Fe_3O_4/ITO was compared with other enzymatic H_2O_2 biosensors, as for the aspects of electrode modification method, linear range, detection limit and sensitivity, which were listed in Table 1. It was revealed that our biosensor showed wider linear range, lower detection limit and much higher sensitivity, which might be due to that the nanocomposite of AuNPs/SPAN@Fe_3O_4 could increase effective surface area and improve electric conductivity. Furthermore, comparing with the extra electro-active probe molecules added in solution, the embedded SPAN could prevent the substrate solution from being contaminated.

Fig. 8

Table 1

441

442 *Reproducibility and stability of the biosensor*

443 The reproducibility and storage stability are the two important parameters for the
444 evaluation of the performance of a biosensor. The detection reproducibility of
445 Nf/HRP-AuNPs/SPAN@Fe_3O_4/ITO in the online assay for ten repetitive injections of
446 0.5 mM H_2O_2 with the RSD of 2.6 % was obtained. The electrode-to-electrode
447 reproducibility was also examined between five different electrodes in 0.5 mM H_2O_2
448 solution, and the RSD was calculated to be 3.5 %. The stability of the biosensor was
449 evaluated by recording the response current for 0.5 mM H_2O_2 over 6 weeks. A
450 constant current response was noticed for the first 3 weeks. After 4 weeks, the current
451 response decreased to 95 %. After 6 weeks, the current response retained about 80 %.
452 Good reproducibility and stability of the biosensor could be attributed to the excellent
453 biocompatibility of AuNPs/SPAN@Fe_3O_4 for preserving the activity of HRP, and the
454 great film-forming ability of Nf/HRP-AuNPs/SPAN@Fe_3O_4 that could be attached on
455 the surface of ITO through magnetic strength.

456

457 *Interference study*

458 Discrimination of interfering species having electro-activities similar to the target
459 analyte is one of the most important analytical aspects for an amperometric biosensor.
460 AA and UA are the most common interfering electro-active species during the
461 amperometric detection of H_2O_2. The interference determination was investigated by
462 comparing the responses between before and after adding of AA and UA, respectively

and together. The changes of the response current could be neglected. This result revealed that the tested interferon could not cause any observable interference for the determination of H_2O_2 at a potential of –0.10 V, indicating high selectivity.

Application of the biosensor to H_2O_2 samples

The concentration of H_2O_2 in commercial disinfector was determined for investigating the possible application of our proposed biosensor for real sample analysis. The disinfector sample was diluted to different concentrations with pH 6.0 PBS buffer. For comparison, the potassium permanganate titration method as a standard method for H_2O_2 detection had been presented. The results obtained with these two methods were given in Table 2. The results determined by the H_2O_2 biosensor were in satisfactory agreement with those obtained by the titration method, implying that the potential application of the proposed H_2O_2 biosensor in real samples.

Table 2

Conclusion

Multifunctional core/shell AuNPs/SPAN@Fe_3O_4 nanocomposites with biocompatibility, electro-activity, conductivity and magnetism have been successfully synthesized through a simple chemical method. The obtained products retained the superparamagnetic properties, while the blocking temperature decreased compared to that of the pure Fe_3O_4 nanoparticles, so the dipole-dipole interactions between the

485 magnetic particles decreased, which will decrease the rate of aggregation of
486 nanoparticles and prolong their life span. By applying a relatively low magnetic field
487 gradient, HRP-AuNPs/SPAN@Fe_3O_4 biocomposites were immobilized onto the
488 surface of an ITO electrode, exhibiting effective electrocatalysis for the reduction of
489 H_2O_2, which shows a new applicable prospect for EAMNC in fabricating a new kind
490 of biosensor.
491

492 ## Acknowledgements

493 We greatly appreciate the support from the National Natural Science Foundation of
494 China (20905035) and Specialized Research Fund for the Doctoral Program of Higher
495 Education (20101106120033). This work is also supported by Overseas Training
496 Program of Education Department of Jiangsu Province.
497
498
499
500
501
502
503
504
505
506

References

[1] I. Rabias, M. Fardis, E. Devlin, N. Boukos, D. Tsitrouli, G. Papavassiliou. No aging phenomena in ferrofluids: The influence of coating on interparticle interactions of maghemite nanoparticles, ACS Nano 2 (2008) 977-983.

[2] Z. H. Xu, C. X. Li, X. J. Kang, D. M. Yang, P. P. Yang, Z. Y. Hou, J. Lin, Synthesis of a multifunctional nanocomposite with magnetic, mesoporous, and Near-IR absorption properties, J. Phys. Chem. C 114 (2010) 16343-16350.

[3] S. H. Hu, X. H. Gao, Nanocomposites with spatially separated functionalities for combined imaging and magnetolytic therapy, J. Am. Chem. Soc. 132 (2010) 7234-7237.

[4] G. Z. Ren, S. J. Zeng, J. H. Hao, Tunable multicolor upconversion emissions and paramagnetic property of monodispersed bifunctional lanthanide-doped $NaGdF_4$ nanorods, J. Phys. Chem. C 115 (2011) 20141-20147.

[5] S. Nayak, K. Harms, S. Dehnen, A new three-dimensional microporous metal-organic framework with heterometallic [Fe-Ag] building units: Synthesis, crystal structure and functional studies, Inorg. Chem. 50 (2011) 2714-2716.

[6] Y. Zhao, B. D. Xi, Y. R. Li, M. F. Wang, Z. A. Zhu, X. F. Xia, L. Y. Zhang, L. J. Wang, Z. K. Luan, Removal of phosphate from wastewater by using open gradient superconducting magnetic separation as pretreatment for high gradient superconducting magnetic separation, Sep. Purif. Technol. 86 (2012) 255-261.

[7] V. Salgueirino-Maceira, M. A. Correa-Duarte, M. Spasova, L. M. Liz-Marzán, M. Farle, Composite silica spheres with magnetic and luminescent functionalities,

529 Adv. Funct. Mater. 16 (2006) 509-514.

530 [8] H. L. Liu, C. H. Sonn, J. H. Wu, K. M. Lee, Y. K. Kim, Synthesis of
531 streptavidin-FITC-conjugated core-shell Fe_3O_4-Au nanocrystals and their
532 application for the purification of CD4 lymphocytes, Biomaterials 29 (2008)
533 4003-4011.

534 [9] J. D. Qiu, H. P. Peng, R. P. Liang, X. H. Xia, Facile preparation of magnetic
535 core–shell Fe_3O_4@Au nanoparticle/myoglobin biofilm for direct
536 electrochemistry, Biosen. Bioelectron. 25 (2010) 1447-1453.

537 [10] H. Ai, Layer-by-layer capsules for magnetic resonance imaging and drug delivery,
538 Adv. Drug Deliv. Rev. 63 (2011) 772-788.

539 [11] E. S. Jang, J. H. Shin, G. Ren, M. J. Park, K. Cheng, X. Y. Chen, J. C. Wu, J. B.
540 Sunwoo, Z. Cheng, The manipulation of natural killer cells to target tumor sites
541 using magnetic nanoparticles, Biomaterials 33 (2012) 5584-5592.

542 [12] P. Govindaiah, T. Hwang, H. Yoo, Y. S. Kim, S. J. Lee, S. W. Choi, J. H. Kim,
543 Synthesis and characterization of multifunctional Fe_3O_4/poly (fluorescein
544 O-methacrylate) core/shell nanoparticles, J. Colloi. Interf. Sci. 379 (2012) 27-32.

545 [13] J. R. Meng, C.Y. Shi, B.W. Wei, W. J. Yu, C. H. Deng, X. M. Zhang, Preparation
546 of Fe_3O_4@C@PANI magnetic microspheres for the extraction and analysis of
547 phenolic compounds in water samples by gas chromatography–mass
548 spectrometry, J. Chromatogr. A. 1218 (2011) 2841-2847.

549 [14] S. Wang, H. M. Bao, P. Y. Yang, G. Chen. Immobilization of trypsin in
550 polyaniline-coated nano-Fe_3O_4/carbon nanotube composite for protein digestion,

Anal. Chim. Acta. 612 (2008) 182-189.

[15] S. H Xuan, Y. X. J Wang, J. C. Yu, K. C. F. Leung, Preparation, characterization, and catalytic activity of core/shell Fe_3O_4@Polyaniline@Au nanocomposites, Langmuir. 25 (2009) 11835-11843.

[16] L.Yan, J. Luo, Q. Fan, M. Suzuki, I. S. Suzuki, M. H. Engelhard, Y. H. Lin, N. Kim, J. Q. Wang, C. J. Zhong, Monodispersed core–shell Fe_3O_4@Au nanoparticles, J. Phys. Chem. B 109 (2005) 21593-21601.

[17] H. Deng, X. L. Li, X. Peng, X. Wang, J. P. Chen, Y. D. Li, Monodisperse magnetic single-crystal ferrite microspheres, Angew. Chem. Int. Ed. 44 (2005) 2782-2785.

[18] R. D. Waldron, Infrared Spectra of Ferrites, Phys. Rev. 99 (1955) 1727-1735.

[19] G. Zhao, J. J. Feng, Q. L. Zhang, S. P. Li, H. Y. Chen, Synthesis and characterization of prussian blue modified magnetite nanoparticles and its application to the electrocatalytic reduction of H_2O_2, Chem. Mater. 17 (2005) 3154-3159.

[20] K. Itaya, I. Uchida, V. D. Neff, Electrochemistry of polynuclear transition metal cyanides: Prussian blue and its analogues, Acc. Chem. Res. 19 (1986) 162-168.

[21] X. J. Chen, Z. X. Chen, J. W. Zhu, C. B. Xu, W. Yan, C. Yao, A novel H_2O_2 amperometric biosensor based on gold nanoparticles/self-doped polyaniline nanofibers, Bioelectrochemistry 82 (2011) 87-94.

[22] V. S. Zaitsev, D. S. Filimonov, I. A. Presnyakov, R. J. Gambino, B. Chu, Physical and chemical properties of magnetite and magnetite-polymer nanoparticles and

573 their colloidal dispersions, J. Colloid. Interface. Sci. 212 (1999) 49-57.

574 [23] X. X. Zhang, Magnetic relaxation and quantum tunneling of magnetization, Adv.

575 Magn. Mater. 1 (2006) 147-181.

576 [24] H. Y. Zhao, W. Zheng, Z. X. Meng, H. M. Zhou, X. X. Xu, Z. Li, Y. F. Zheng,

577 Bioelectrochemistry of hemoglobin immobilized on a sodium alginate- multiwall

578 carbon nanotubes composite film, Biosens. Bioelectron. 24 (2009) 2352-2357.

579 [25] H. S. Yina, S. Y. Ai, W. J Shi, L. S Zhu, A novel hydrogen peroxide biosensor

580 based on horseradish peroxidase immobilized on gold nanoparticles-silk fibroin

581 modified glassy carbon electrode and direct electrochemistry of horseradish

582 peroxidase. Sens. Actuators, B 137 (2009) 747-753.

583 [26] C. Xiang, Y. Zou, L. Sun, F. Xu, Direct electrochemistry and enhanced

584 electrocatalysis of horseradish peroxidase based on flowerlike ZnO-gold

585 nanoparticle-Nafion nanocomposite, Sens. Actuators B 136 (2009) 158-162.

586 [27] M. Zhu, S. B. Han, Z. B. Yuan, β-Cyclodextrin polymer as the immobilization

587 matrix for peroxidase and mediator in the fabrication of a sensor for hydrogen

588 peroxide, J. Electroanal. Chem. 480 (2000) 255-261.

589 [28] Y. Xin, F. B. Xiao, H. W. Lin, F. Wu, D. Z. Chen, Z. Y. Wu, A novel H_2O_2

590 biosensor based on Fe_3O_4-Au magnetic nanoparticles coated horseradish

591 peroxidase and graphene sheets-Nafion film modified screen-printed carbon

592 electrode, Electrochim. Acta 109 (2013) 750-755.

593

594

595

596

597

598

Figure Legends

Fig. 1. (A-C) TEM and (D-F) FESEM images of Fe_3O_4, SPAN@Fe_3O_4 and AuNPs/SPAN@Fe_3O_4 samples.

Fig. 2. (A) XRD patterns and (B) FT-IR spectra of the as-prepared (a) Fe_3O_4, (b) SPAN@Fe_3O_4 and (c) AuNPs/SPAN@Fe_3O_4 nanoparticles. (C) UV-Vis absorption spectra of the colloidal Au solution (a) before and (b) after magnetic separation of reacted AuNPs/SPAN@Fe_3O_4 nanocomposites. (D) EDS spectra of the AuNPs/SPAN@Fe_3O_4 nanocomposites with core-shell structure.

Fig. 3. TGA curves for (a) SPAN@Fe_3O_4 and (b) AuNPs/SPAN@Fe_3O_4 nanocomposites.

Fig. 4. (A) Magnetization measurements as a function of applied magnetic field for (a) pure Fe_3O_4, (b) SPAN@Fe_3O_4 and (c) AuNPs/SPAN@Fe_3O_4 at 300 K. Inset of (A) shows the data plotted over the low field range. (B) ZFC at 100 Oe and FC measurements of these three samples.

Fig. 5. (A) Cyclic voltammograms of the AuNPs/SPAN@Fe_3O_4/ITO at 20, 50, 100, 200, 300, 400, 500 and 600 mV s^{-1} (from internal to external) in 0.1 M pH 6.0 PBS. Inset shows the photographs of the plots of the peak current vs. $v^{1/2}$ (B) CVs of AuNPs/SPAN@Fe_3O_4 in solutions with different pH values at 100mV s^{-1}. Inset:

amplified curves of pH 6 and 7. (C) Contact angels of water on (a) pure Fe_3O_4, (b) AuNPs/SPAN@Fe_3O_4 nanocomposites and (c) HRP-AuNPs/SPAN@Fe_3O_4 bioconjugates.

Fig. 6. (A) CV and (B) EIS characterization of different modified electrodes: (a) bare ITO, (b) Nf/AuNPs/SPAN@Fe_3O_4/ITO, (c) Nf/HRP-AuNPs/SPAN@Fe_3O_4/ITO in 0.1 M KCl solution containing 5 mM $[Fe(CN)_6]^{3-/4-}$ at a scan rate of 100 mVs^{-1}.

Fig. 7. Dependence of amperometric response of 0.5 mM H_2O_2 in 0.1 M PBS at Nf/HRP-AuNPs/SPAN@Fe_3O_4/ITO electrode on the (A) HRP dosage, (B) solution pH, (C) working potential and (D) temperature.

Fig. 8. (A) Amperometric response of Nf/HRP-AuNPs/SPAN@Fe_3O_4/ITO electrode (a) in the absence and (b-j) upon addition of 0.05, 0.10, 0.15, 0.25, 0.35, 0.85, 1.35, 1.85, 2.25 mM H_2O_2 into 0.1 M pH 6.0 PBS containing at −0.10 V. (B) calibration curve.

Figure 1

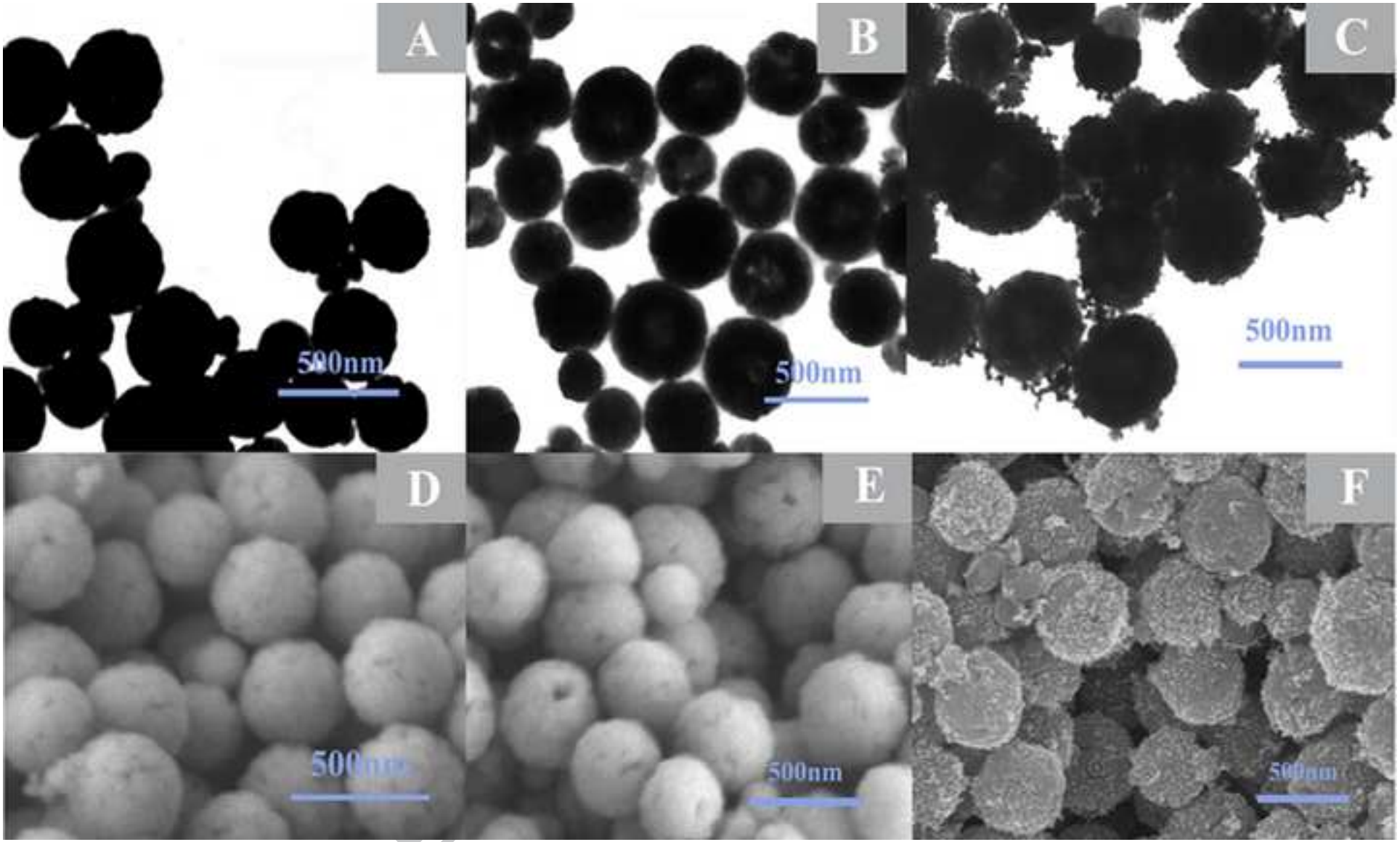

Figure 2

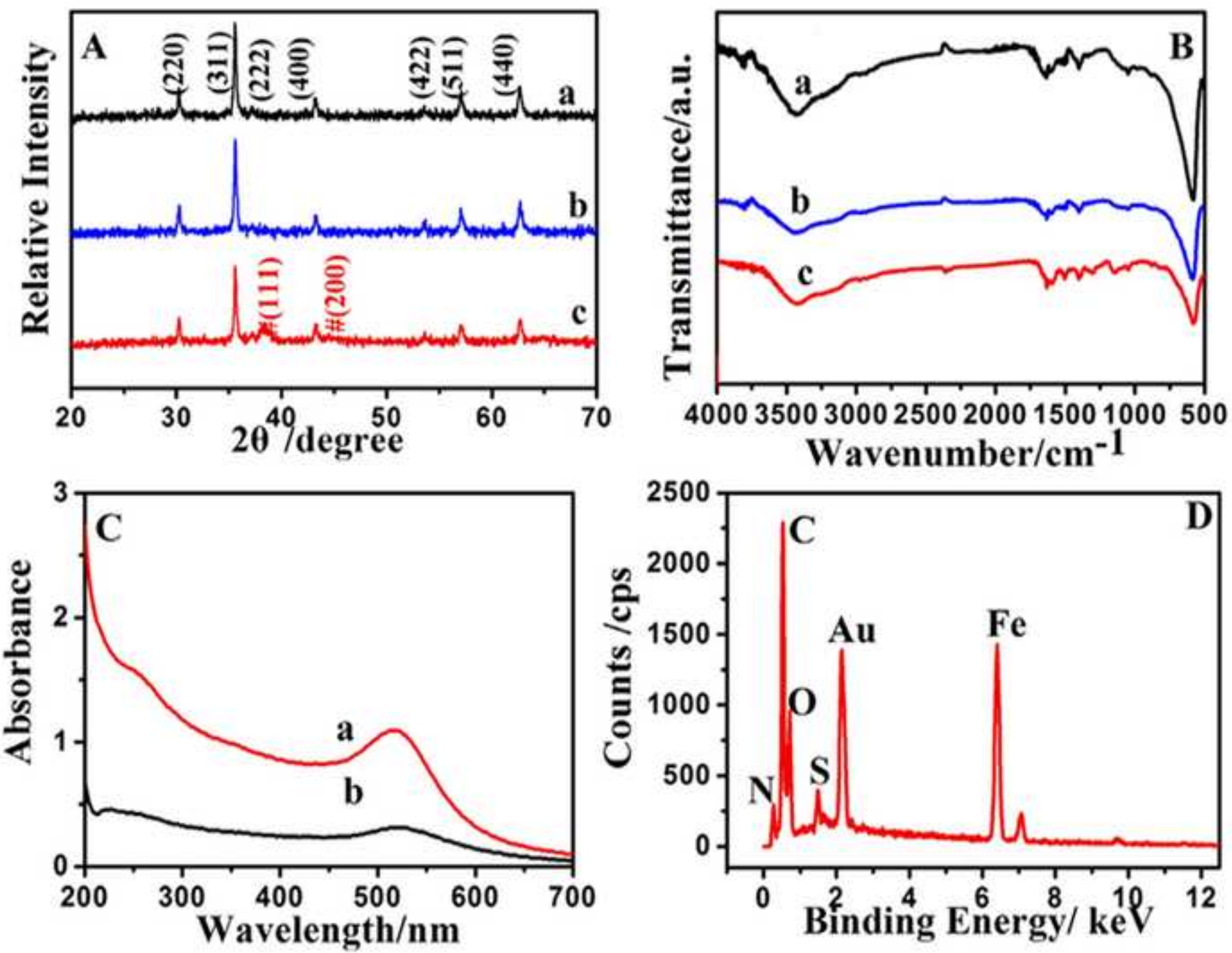

Figure 3

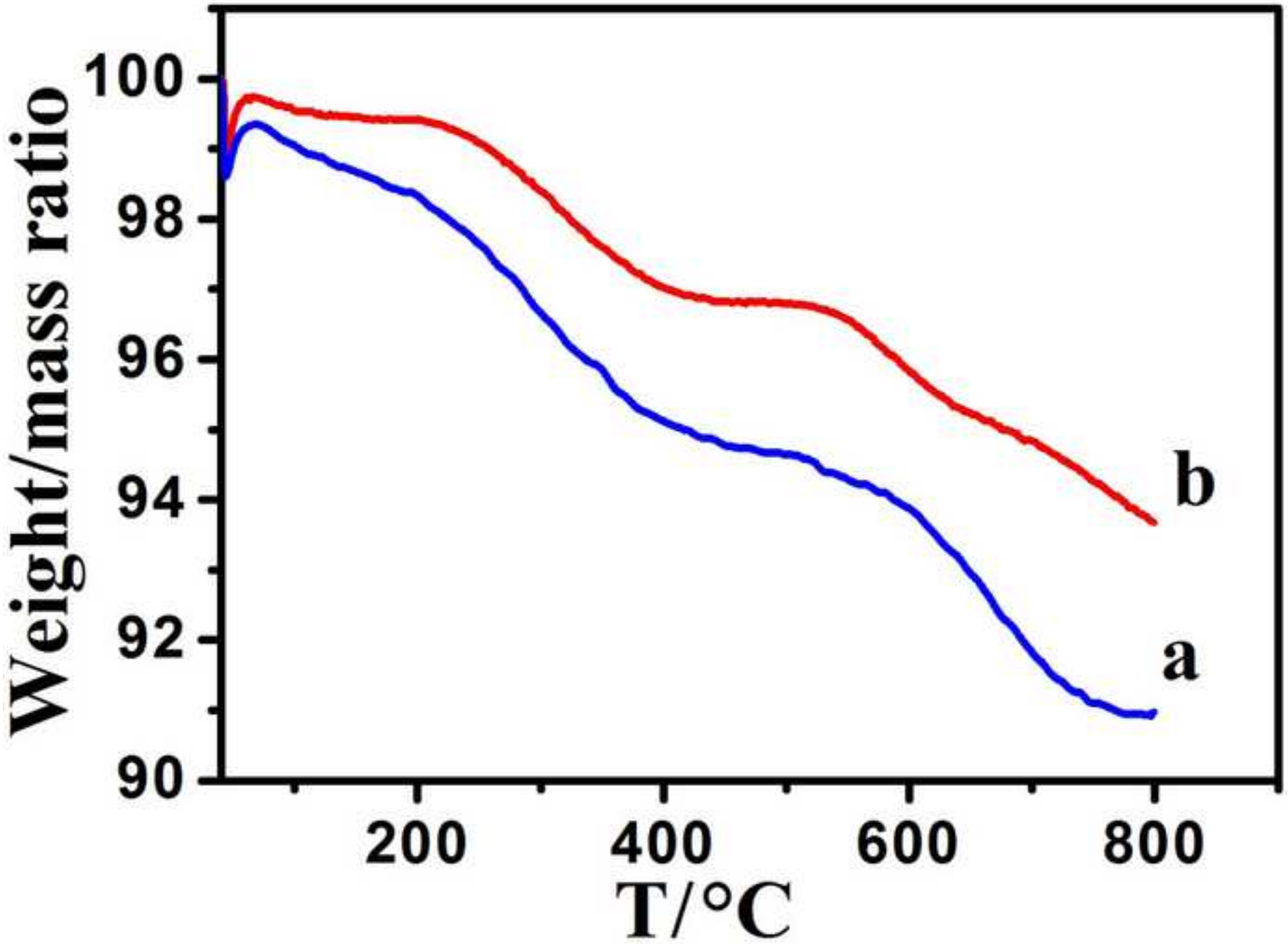

Figure 4

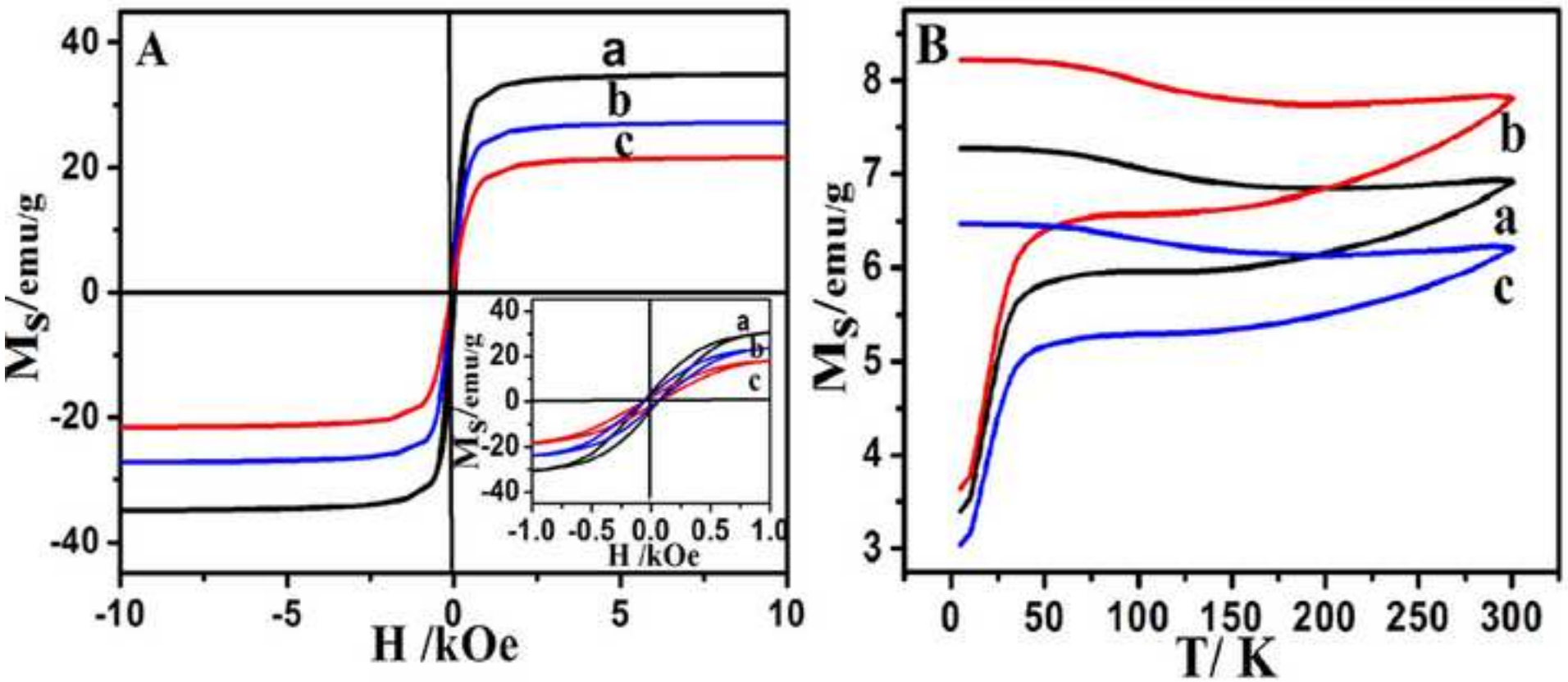

Figure 5

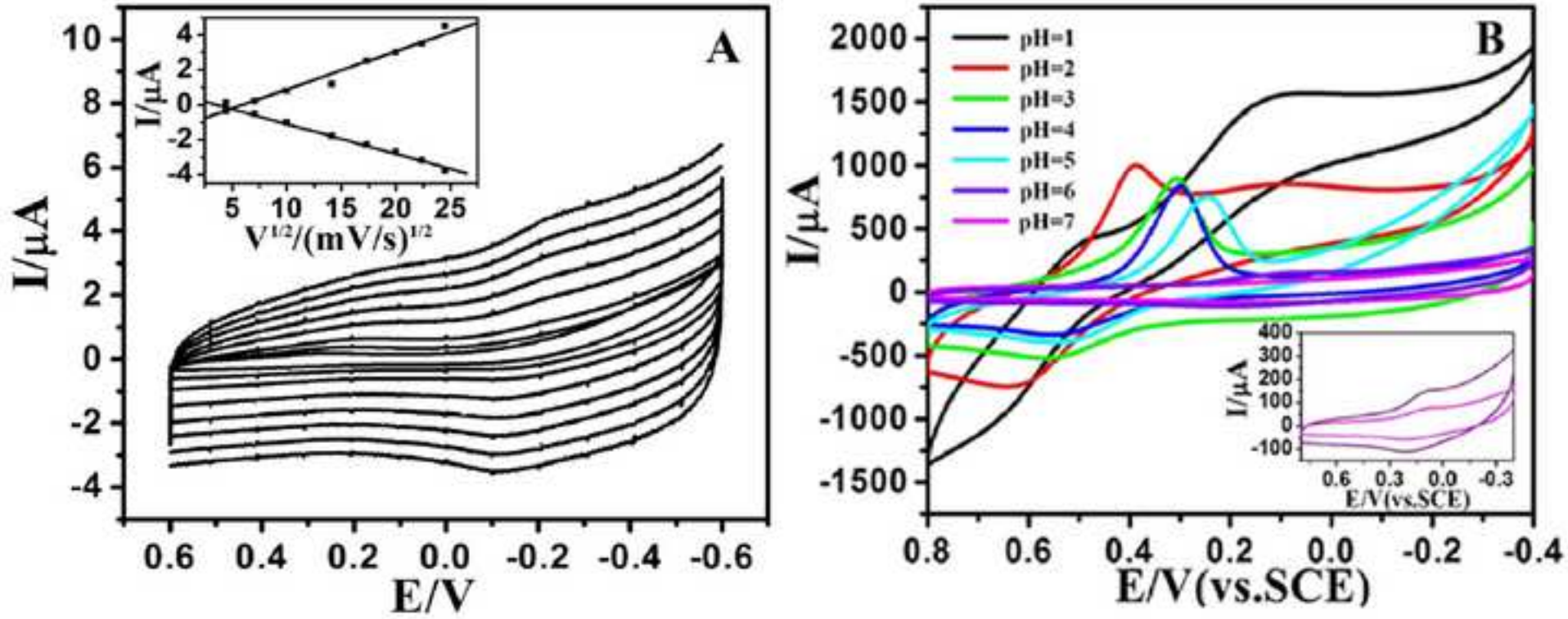

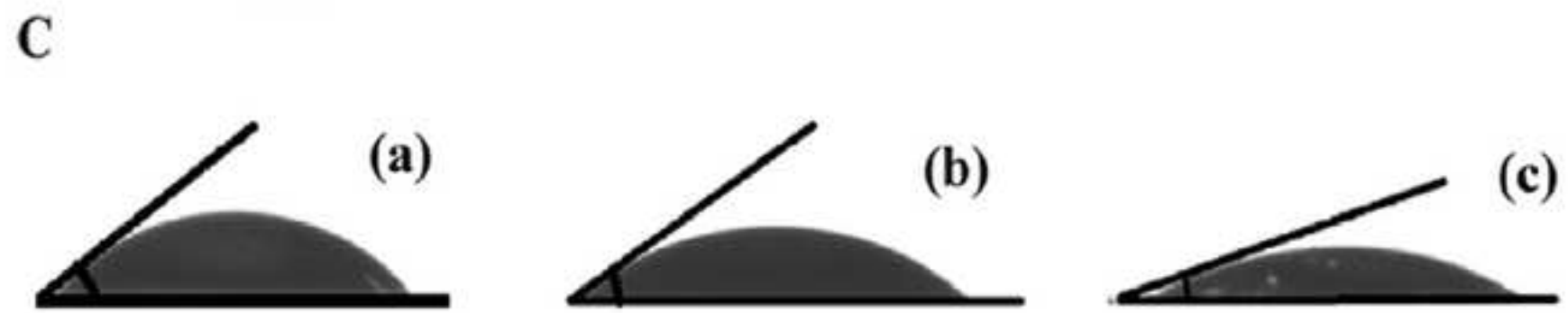

Figure 6

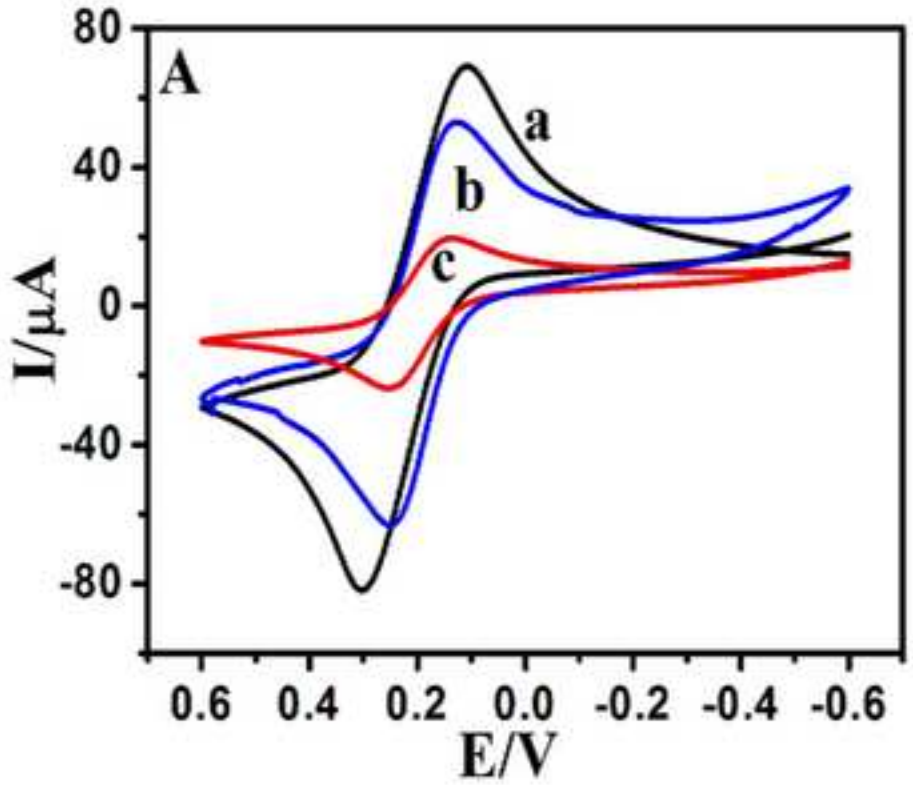

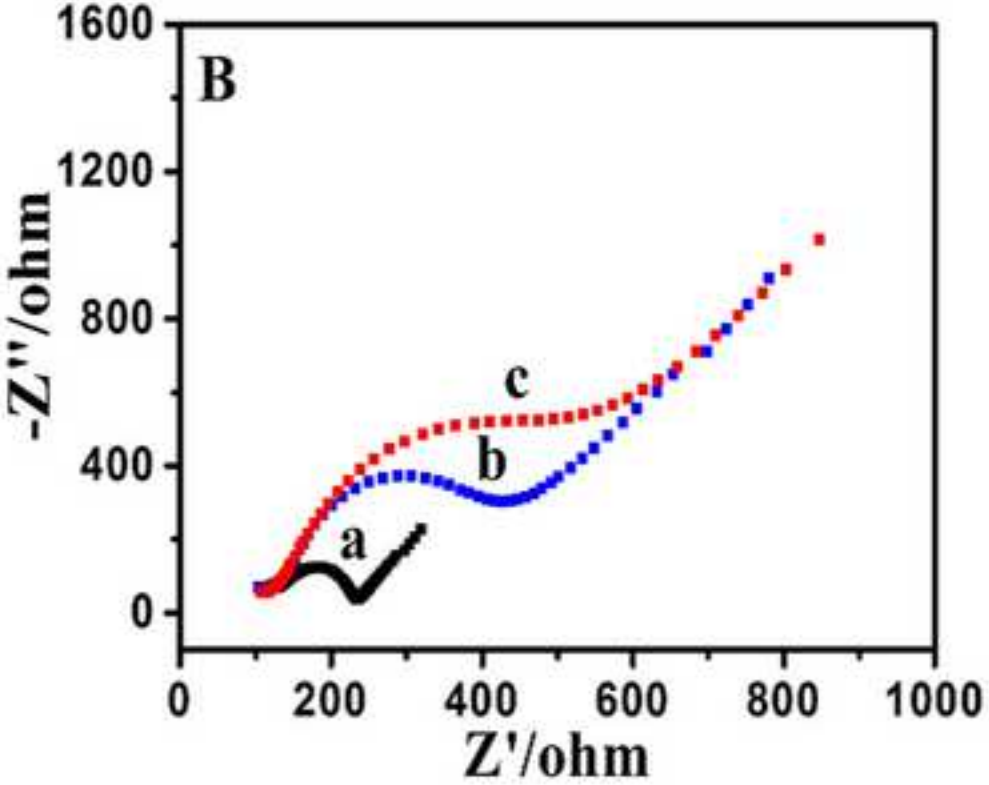

Figure 7

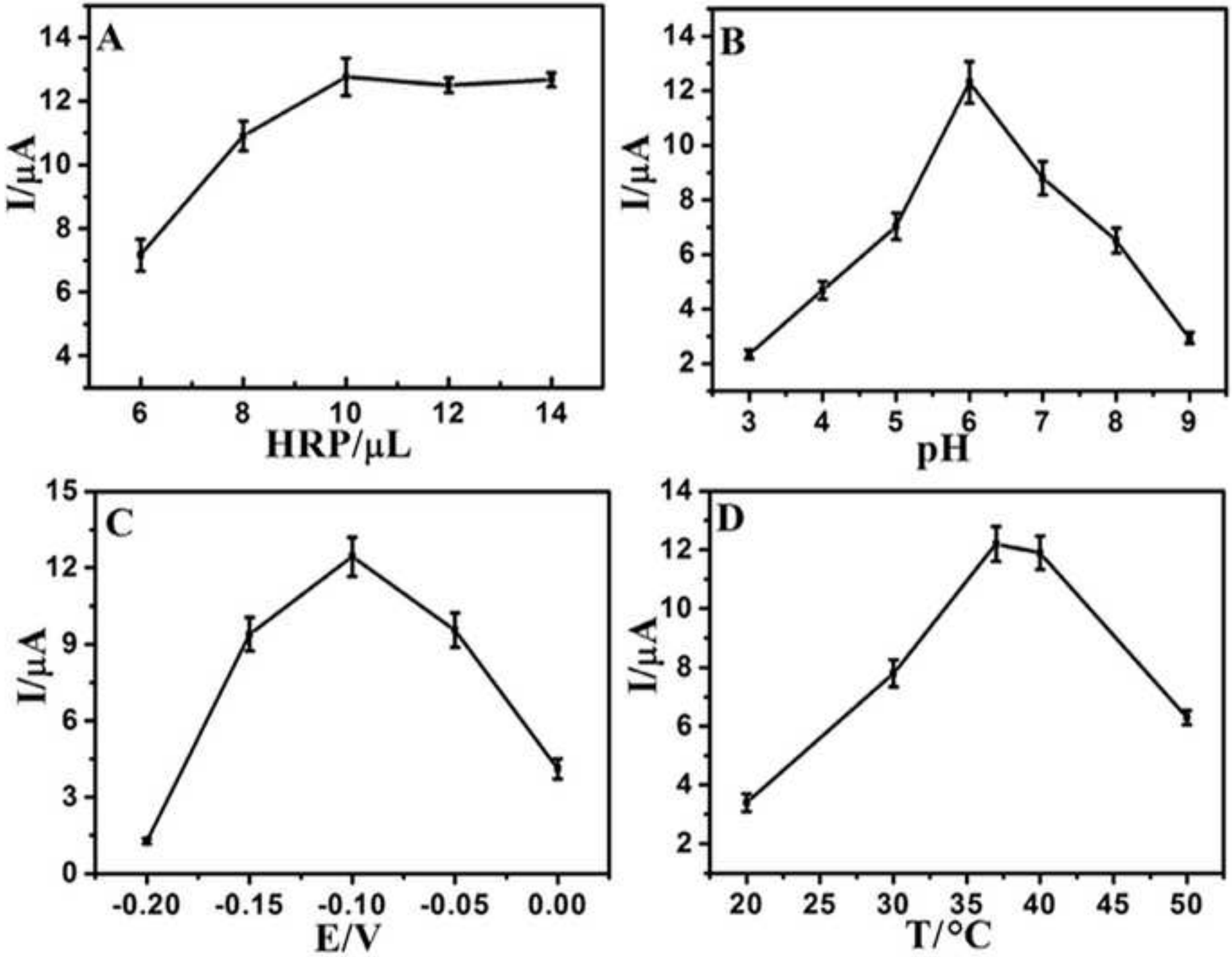

Figure 8

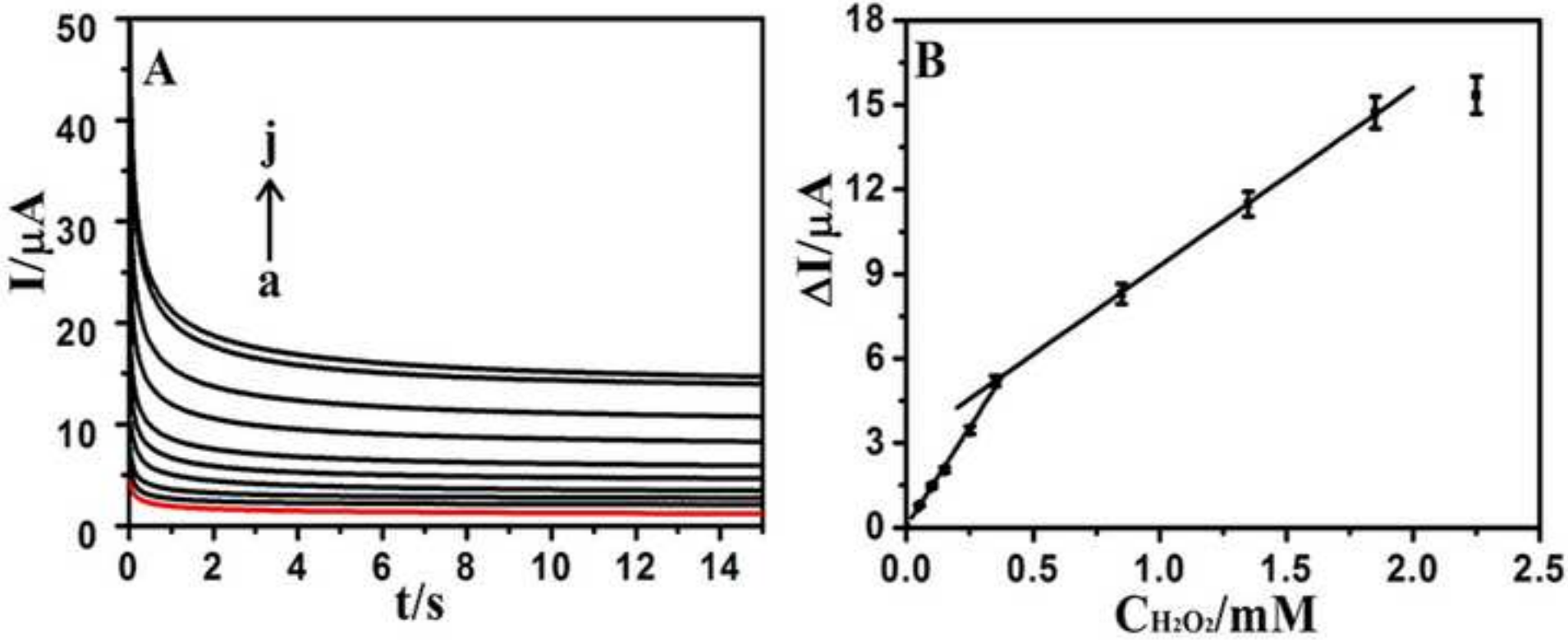

643 **Table 1.** The comparison of different enzymatic H_2O_2 biosensors

Modified electrode	Linear range / mM	Detection limit / μM	Sensitivity/ μA mM^{-1} cm^{-2}	Ref.
Hb/SA-MWCNTs/GCE	0.04–0.2	16.4	0.23	[24]
HRP–AuNPs–SF/GCE	0.01-1.8	5	-	[25]
HRP–ZnO–GNPs–Nafion/GCE	0.015-1.1	9	-	[26]
β-CDP-cationic dye-HRP/GCE	1.0–1.1	50	-	[27]
SPCE/GS-Nafion/Fe_3O_4-Au-HRP	0.02-2.5	12	68.6	[28]
Nf/HRP-AuNPs/SPAN@Fe_3O_4/ITO	0.05-0.35, 0.35-1.85	10	199.9, 84.3	this work

644

645

646

647 **Table 2.** Detection of H_2O_2 in disinfector samples by the proposed biosensor and
648 standard titration method

Sample	Titration method / mM	Biosensor / mM	RSD / %
1	0.126	0.124	-1.59
2	0.225	0.219	-2.67
3	1.178	1.193	+1.27

649

650